Cell Reports
Physical Science

CellPress
OPEN ACCESS

Article

Single photovoltaic material solar cells with enhanced exciton dissociation and extended electron diffusion

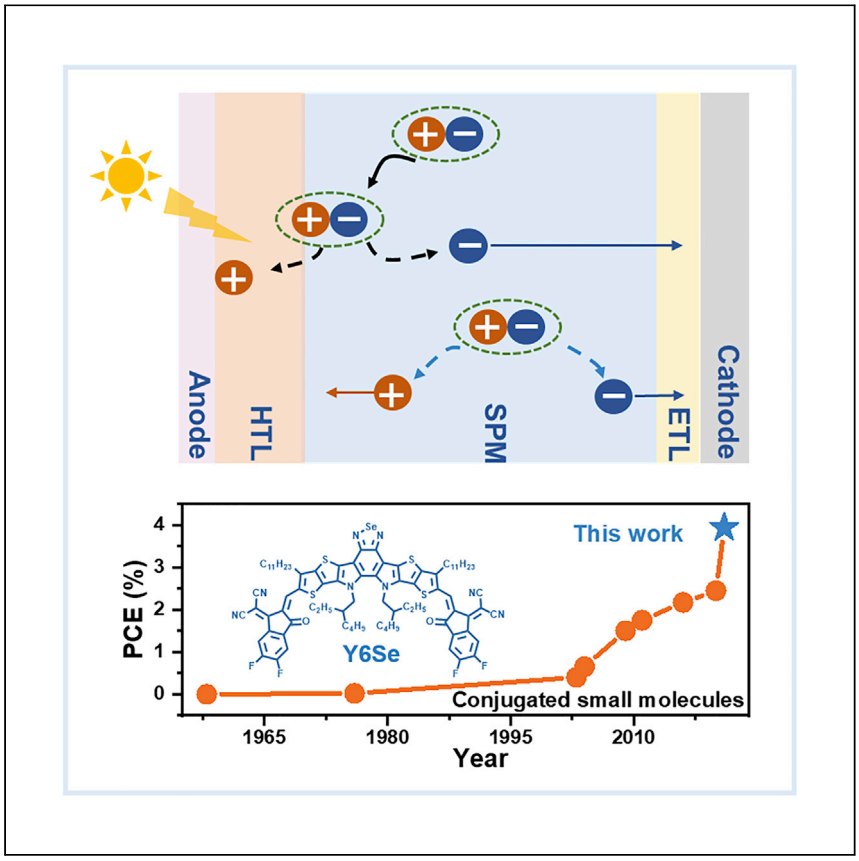

Typical organic photovoltaic semiconductors exhibit high exciton binding energy, hindering the development of organic solar cells based on single photovoltaic materials (SPM-OSCs). Zhang et al. report that Y6Se exhibits enhanced exciton dissociation and extended electron diffusion length, leading to enhanced device efficiency in SPM-OSCs.

Zhenzhen Zhang, Li Li, Chaoying Xu, ..., Ye Yang, Weigao Xu, Yuze Lin

xuwg@nju.edu.cn (W.X.)
linyz@iccas.ac.cn (Y.L.)

Highlights

Enhanced exciton dissociation and extended electron diffusion exist in Y6Se

The 3.94% efficiency is higher than those reported for SPM-OSCs with D-A molecules

SPM-OSCs show superior thermal stability than typical bulk heterojunction OSCs

Zhang et al., Cell Reports Physical Science 3, 100895
June 15, 2022
https://doi.org/10.1016/j.xcrp.2022.100895

Please cite this article in press as: Zhang et al., Single photovoltaic material solar cells with enhanced exciton dissociation and extended electron diffusion, Cell Reports Physical Science (2022), https://doi.org/10.1016/j.xcrp.2022.100895

Cell Reports
Physical Science

CellPress
OPEN ACCESS

Article

Single photovoltaic material solar cells with enhanced exciton dissociation and extended electron diffusion

Zhenzhen Zhang,[1,4,5] Li Li,[2,5] Chaoying Xu,[3] Pengfei Jin,[1,4] Miaofei Huang,[1,4] Yawen Li,[1,4] Hong Wang,[1,4] Yuanping Yi,[1,4] Chuang Zhang,[1,4] Ye Yang,[3] Weigao Xu,[2,*] and Yuze Lin[1,4,6,*]

SUMMARY

Typical organic photovoltaic semiconductors exhibit high exciton binding energy (E_b, typically >300 meV), hindering the development of organic solar cells based on a single photovoltaic material (SPM-OSCs). Herein, compared with the control molecule (Y6), Y6Se with selenium substitution exhibits reduced E_b and faster relaxation of the exciton state or the intermediate intra-moiety excimer state, indicating that the exciton dissociation in Y6Se film can be driven by lower energy. The SPM-OSCs based on Y6Se film without and with 1 wt % p-type polymer additive exhibit long charge-carrier lifetime, and extended electron diffusion length, leading to impressive power conversion efficiencies of 3.07% and 3.94%, respectively, which are significantly higher than those values reported for SPM-OSCs based on single photovoltaic small molecules in the literature. In addition, the SPM-OSCs based on Y6Se show superior thermal stability, relative to the typical bulk heterojunction OSCs based on Y6Se blending with polymer donor.

INTRODUCTION

Organic solar cells (OSCs) have attracted considerable attention due to their advantages, including low cost, flexibility, and solution processing.[1–5] Recently, power conversion efficiencies (PCEs) greater than 18% have been achieved in bulk heterojunction (BHJ) OSCs, with active layers fabricated by blending donor and acceptor materials.[6,7] Compared with high-performance inorganic/hybrid counterparts, typical organic photovoltaic materials exhibit high exciton binding energy (E_b).[8,9] This results in unavoidable energy losses, although the additional interface energy offset in BHJ active layers can promote exciton dissociation.[10,11] In addition, the complexity of the blended active layers has made the study of the mechanism more complicated, and BHJ-OSC active layers suffer from morphological instability, which hampered the commercialization of OSCs.[12–15] In comparison, single photovoltaic materials (SPM-OSCs), which are composed of a single component as photoactive material that generates and transports free charge carriers, present some advantages, such as simpler device structures and a more stable active layer morphology with smaller energy disorder, which should result in a higher upper limit of device efficiency and stability (Scheme 1A).[16] Different from the exciton dissociation process at the donor/acceptor interface and electron and hole transport along the acceptor and donor phases within active layer blend of BHJ-OSCs (Scheme 1B), respectively, free charge carriers are generated in SPM-OSCs in two ways. Excitons spontaneously dissociate aided by the built-in field or interfacial dipole effect at the contact layer/active layer interface, and then both the hole and electron transported

[1]Beijing National Laboratory for Molecular Sciences, CAS Key Laboratory of Organic Solids and Laboratory of Photochemistry, Institute of Chemistry, Chinese Academy of Sciences, Beijing 100190, China

[2]Key Laboratory of Mesoscopic Chemistry, School of Chemistry and Chemical Engineering, Nanjing University, Nanjing 210023, China

[3]State Key Laboratory of Physical Chemistry of Solid Surfaces, College of Chemistry and Chemical Engineering, Xiamen University, Xiamen 361005, China

[4]University of Chinese Academy of Sciences, Beijing 100049, China

[5]The authors contributed equally

[6]Lead contact

*Correspondence: xuwg@nju.edu.cn (W.X.), linyz@iccas.ac.cn (Y.L.)

https://doi.org/10.1016/j.xcrp.2022.100895

Please cite this article in press as: Zhang et al., Single photovoltaic material solar cells with enhanced exciton dissociation and extended electron diffusion, Cell Reports Physical Science (2022), https://doi.org/10.1016/j.xcrp.2022.100895

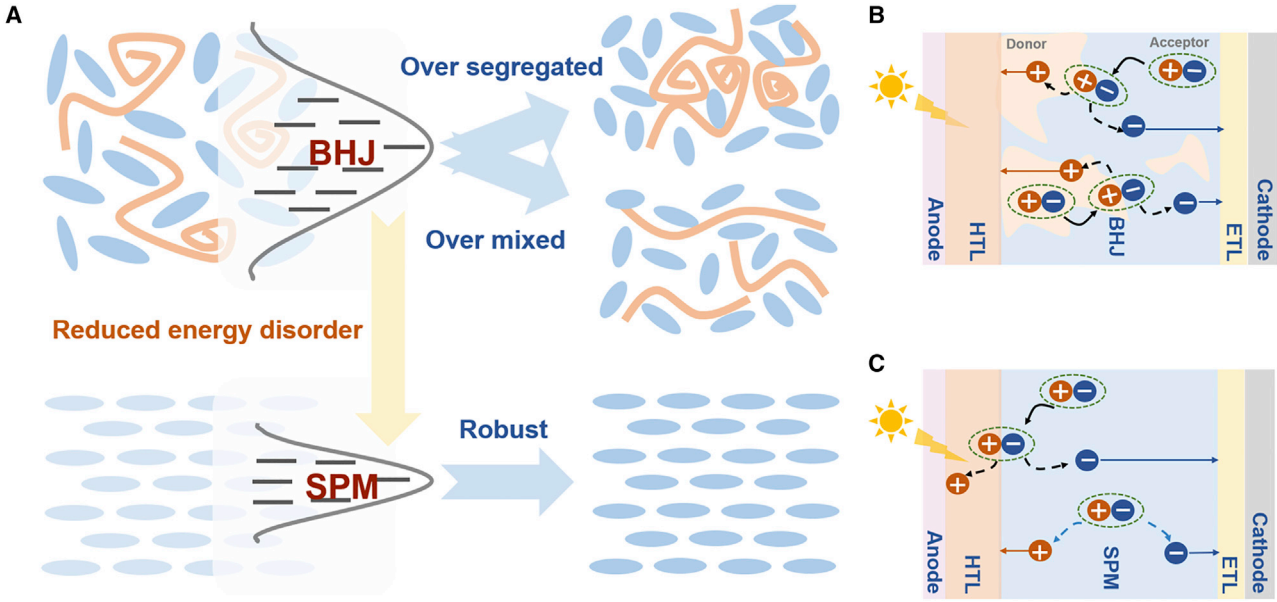

Scheme 1. The diagram of study motivation and device work mechanism

(A) Relative to BHJ-OSCs, the SPM-OSCs with simpler device structures exhibit smaller energy disorder and more stable active layer morphology, which indicates a higher upper limit of device efficiency and stability. BHJ is bulk heterojunction, SPM is single photovoltaic material, the orange lines stand for polymer donors, and blue ellipses stand for small molecule electron acceptors. Charge-generation and charge-transport process in (B) BHJ-OSCs and (C) SPM-OSCs. Black solid arrow: exciton diffusion. Black dotted arrows: exciton dissociation at interface. Blue dotted arrows: exciton spontaneous dissociation. Blue solid arrows: electron transport. Orange solid arrow: hole transport. HTL, hole transporting layer; ETL, electron transporting layer.

in SPM-OSCs along single component material to the anode and cathode with the contact layers, respectively (Scheme 1C). Low-energy-driven exciton dissociation and high free charge-carrier transport/diffusion properties are important to achieve high-performance SPM-OSCs. However, the low efficiency of exciton dissociation within pristine organic semiconductors (E_b typically >300 meV)[8] has severely limited the development of SPM-OSCs. At present, the active layer materials developed for SPM-OSCs mainly include D-A conjugated small molecules,[17,18] block polymers,[19] and double-cable molecules/polymers,[20,21] all of which integrate the electron donating and withdrawing units on the same molecule/polymer through π-π conjugated or flexible alkyl chain in order to boost exciton dissociation.

Compared with block polymers and double-cable molecules/polymers, D-A molecules have simpler chemical structures and/or are easier to be synthesized.[22] With the rapid development of fused ring electron acceptors (FREAs) since 2015,[23–26] very small, even "zero" energy offset was required to achieve effective dissociation of excitons at the interface between electron donors and FREAs.[27–30] Very recently, the theoretical study by Wei, Yi et al. has shown that high-performance FREA (Y6, Figure 1A; full chemical names are provided in Note S1) exhibit small E_b of −0.11∼0.15 eV,[31] while Zhang et al. found that intra-moiety excimer (i-Ex) states, rather than the traditional charge transfer (CT) states, act as the intermediate for the hole transfer channel in Y6-based OSCs.[32] Hodgkiss et al. indicated that free charges exist in equilibrium with excitons in Y6 films.[33] These studies indicate that exciton dissociation with minimal additional driving force may take place in Y6, opening the door for the development of SPM-OSCs. However, there are very few studies on SPM-OSCs with FREAs, and most of them show PCEs lower than 2% (Table S1), for example, Y6-based SPM-OSCs showed PCE of only 0.42% to 1.9%.[18,31]

Please cite this article in press as: Zhang et al., Single photovoltaic material solar cells with enhanced exciton dissociation and extended electron diffusion, Cell Reports Physical Science (2022), https://doi.org/10.1016/j.xcrp.2022.100895

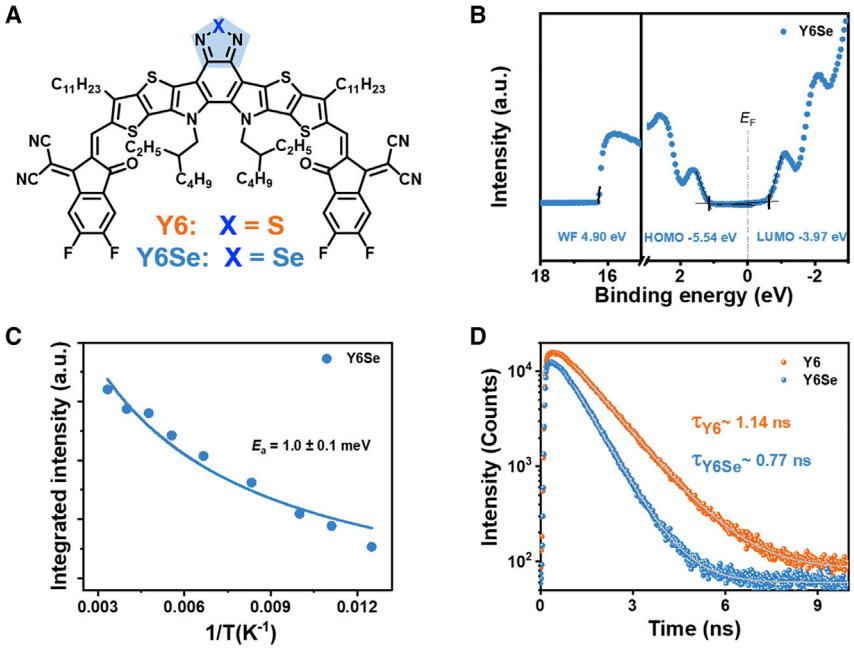

Figure 1. Molecular structures, exciton binding energy, and exciton dissociation kinetics

(A) Molecular structures of the Y6 and Y6Se.

(B) UPS and LEIPS spectra of Y6Se with respect to the Fermi energy level (E_F) at 0 eV (work function [WF] values are labeled).

(C) Integrated PL intensity as a function of temperature from 80 to 300 K for the Y6Se films.

(D) The time-resolved PL spectra for Y6 and Y6Se film.

Here, we focus on SPM-OSCs based on FREAs with a detailed study of the exciton dissociation kinetics and charge-carrier diffusion of Y6 and Y6Se (Figure 1A, full chemical names are provided in Note S1) films by temperature-dependent photoluminescence (PL), transient absorption spectroscopy (TA), magneto-photocurrent (MPC), transient photovoltage (TPV) measurements among others. Compared with Y6 films, Y6Se, with selenium substitution, show a reduced activation energy (E_a of 1.0 meV) of nonradiative state back to exciton state, decreased E_b, longer charge-carrier lifetime, and extended electron diffusion length, leading to higher PCEs in SPM-OSCs with copper thiocyanate (CuSCN)/sodium thiocyanate (NaSCN) as hole transporting layer (HTL). Adding 1wt % polymer additive, the PCE of the SPM-OSCs based on Y6Se achieve to 3.94%, which is much higher than those of the values reported in the literature for SPM-OSCs based on D-A molecules including FREAs. In addition, SPM-OSC devices show much better thermal stability than those traditional BHJ devices.

RESULTS AND DISCUSSION

Exciton binding energy

We have previously demonstrated that Y6Se with selenium substitution exhibited lower energy disorder, more ordered molecular packing, and higher electron mobility than Y6. Then, the BHJ-OSCs based on Y6Se acceptor showed superior performance than that of Y6-based control devices.[25] These results suggest that Y6Se may have potential on SPM-OSCs. One of the key factors to determine the performance of SPM-OSCs is the E_b, which is defined as the difference between the transport gap and optical band gap.[8] Transport gap can be obtained from the difference between the ionization potential (IP) and the electron affinity (EA).[8] Theoretically, it is straightforward to determined E_b in the gas phase by electronic structure

calculations.[34] Y6Se exhibited relatively larger molecular dipole and smaller E_b (0.35 eV) than Y6 (0.36 eV) according to the density functional theory (DFT) and time-dependent DFT (TDDFT) calculations (Table S2). Experimentally, the IP and EA of thin film can be measured by ultraviolet photoelectron spectrometry (UPS) and low-energy inverse photoemission spectrometry (LEIPS), respectively.[35] From the difference of IP and EA, the transport gap of Y6Se thin film was determined to be 1.57 eV (Figure 1B). Y6Se thin film showed an optical band gap of 1.32 eV.[25] As a result, the E_b of Y6Se thin film was 0.25 eV, smaller than the value (0.30 eV) of Y6 thin film obtained by the same method.[36] The joint theoretical and experimental study indicated that Y6Se with reduced E_b required lower driven energy for exciton dissociation than that of Y6 film.

Exciton dissociation kinetics

Then, we further study the exciton dissociation kinetics of neat Y6Se film by temperature-dependent PL spectrometry, and time-resolved photoluminescence (TRPL). As the temperature gradually increases from 80 K to 300 K, the PL peaks of Y6Se are blue-shifted while their PL intensities are enhanced (Figure S1 and 1C).[31] This abnormal phenomenon is consistent with what was observed of Y6 thin film in the recent study by Wei, Yi et al.[31] Here PL was from emissive excitons, which was confirmed by light intensity dependent PL measurement (Figure S2).[37] Along with increasing temperature, the relaxation of nonradiative state back to emissive excitons is facilitated, and the E_a for backward to exciton conversion can be obtained by fitting the temperature dependence of PL intensity I(T) with the Arrhenius Equation 1[38]:

$$\frac{I(T)}{I_0} = 1 + Ae^{(-E_a/k_BT)} \quad \text{(Equation 1)}$$

where I_0 is the intensity at 0 K, k_B is the Boltzmann constant, and T is the sample temperature. Compared with the E_a (18.5 meV) of Y6 thin film calculated by the same method,[31] Y6Se exhibited a much smaller E_a of 1.0 meV, leading to fast inter-conversion between the excitonic state and nonradiative state of Y6Se thin film. This small energy gap benefited free carriers generated after photoexcitation in Y6Se film with minimized additional driving force at room temperature. Then TRPL study revealed Y6Se thin film showed shorter PL lifetime (0.77 ns) than that (1.14 ns) of Y6 thin film (Figure 1D). This phenomenon supported the process of exciton transformation to other state within Y6Se was faster than Y6.

Then, TA measurement was carried out to further confirm the exciton dissociation dynamic process in the Y6 and Y6Se thin films (Figures 2A–2E). Both Y6 and Y6Se thin films display a strong photoinduced absorption band centered at around 1560 nm, which has been attributed to the i-Ex state.[32] This i-Ex state was believed to be the intermediate state in the exciton dissociation and transport in the films. The formation rate of i-Ex absorption in Y6 and Y6Se are similar, while the i-Ex absorption in the former decays slower than that in the latter, which may suggest that the exciton state or the intermediate i-Ex state relaxes faster in the Y6Se film than that in the Y6 film. This phenomenon supported the process of exciton dissociation within Y6Se was faster than Y6, which is consistent with the results of PL and TRPL.

Photovoltaic performance

In view of smaller E_b and faster relaxation of exciton state or the intermediate i-Ex state, Y6Se has more potential in SPM-OSCs than Y6. To demonstrate the application of Y6 and Y6Se in SPM-OSCs, we fabricated SPM-OSCs employing structure of ITO/CuSCN/NaSCN/Y6 or Y6Se neat film/(2-(1,10-phenanthrolin-3-yl)naphth-6-yl)diphenylphosphine oxide (Phen-NaDPO)/Al. CuSCN, an intrinsically p-type

Please cite this article in press as: Zhang et al., Single photovoltaic material solar cells with enhanced exciton dissociation and extended electron diffusion, Cell Reports Physical Science (2022), https://doi.org/10.1016/j.xcrp.2022.100895

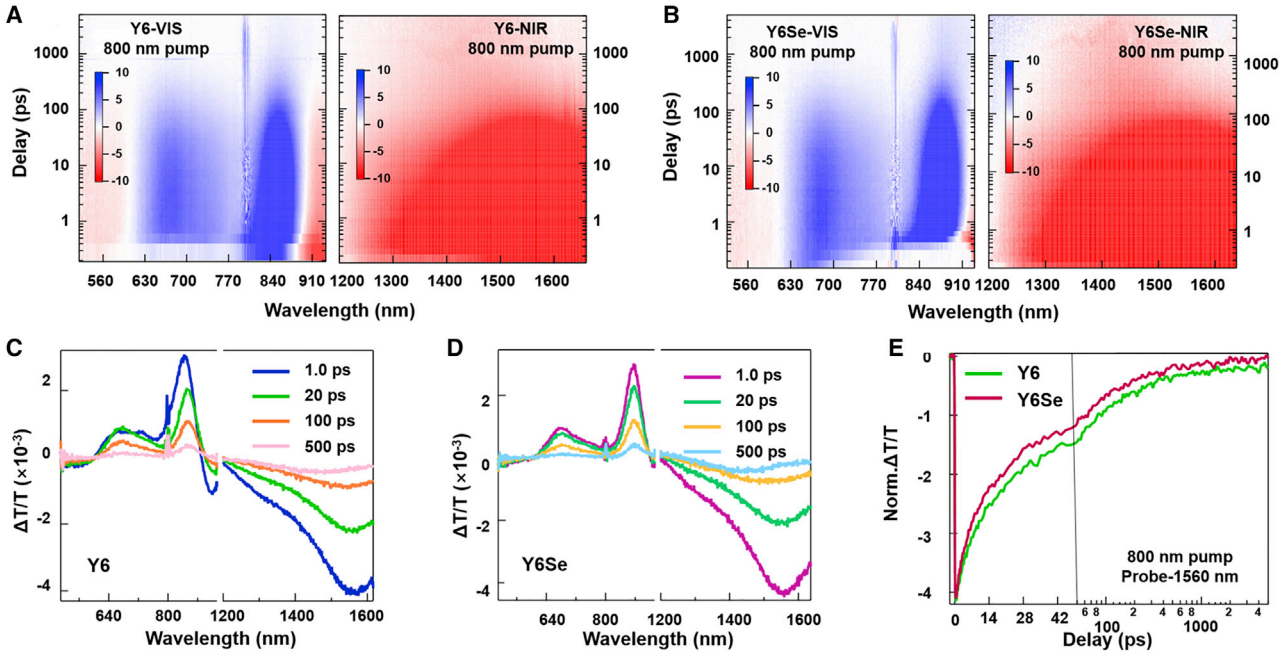

Figure 2. Exciton dissociation kinetics

(A and B) Pseudo-color images of the TA spectra for the neat Y6 film (A) and neat Y6Se film (B). The vertical and horizontal axes represent the delay and probe wavelength, respectively. Both samples were pumped at 800 nm.

(C and D) TA spectra recorded at indicated delays for the neat Y6 film (C) and neat Y6Se film (D).

(E) Comparison between the normalized TA kinetic traces probed at 1,560 nm between the neat Y6 and Y6Se samples.

inorganic semiconductor with the highest occupied molecular orbital (HOMO) energy level of −5.3 eV[39] (Figure 3A), can form heterojunction with Y6 or Y6Se to promote exciton dissociation and hole transfer. Moreover, Nelson et al. demonstrated that photogenerated excitons in organic semiconductors can be effectively converted into free charges through the mediation of CT states at the CuSCN/organic semiconductor interface.[40] It should be pointed out here that although CuSCN is a p-type semiconductor, CuSCN does not contribute photoinduced charge carriers in devices due to its negligible absorption after 325 nm.[41] NaSCN post-treating has been found to improve hole conductivity and reduce trap density of CuSCN film.[42] Phen-NaDPO is a wide bandgap electron-transport layer, which can effectively block holes.[43] The current density-voltage (*J-V*) curves of the SPM-OSCs based on Y6 and Y6Se under the illumination of AM 1.5G, 100 mW cm^{-2} are shown in Figure 3B. The SPM-OSCs based on Y6Se neat film show the optimized PCE of 3.07% with a short circuit current density (J_{SC}) of 7.36 mA cm^{-2}. The detailed photovoltaic data for different Y6Se film thicknesses are shown in Figure S3 and Table S3. In contrast, SPM-OSC based Y6 showed a PCE of 3.03% with J_{SC} of 6.97 mA cm^{-2}. The maximum value of external quantum efficiency (EQE) of CuSCN/NaSCN/Y6Se or Y6 based devices exceeds 28% or 25%, respectively (Figure 3C), indicating that efficient exciton dissociation and free charge generation in CuSCN-based devices.

Mechanism of exciton dissociation

To investigate the mechanism of exciton dissociation in CuSCN-based devices, we fabricated SPM-OSCs by replacing CuSCN/NaSCN with poly(3,4-ethylenedioxythiophene):poly(styrenesulfonate) (PEDOT:PSS), which lacks an appropriate interface for charge separation.[40] As shown in Figure S4A, the EQE spectra of both devices based on Y6 and Y6Se show a photovoltaic response in the whole absorption

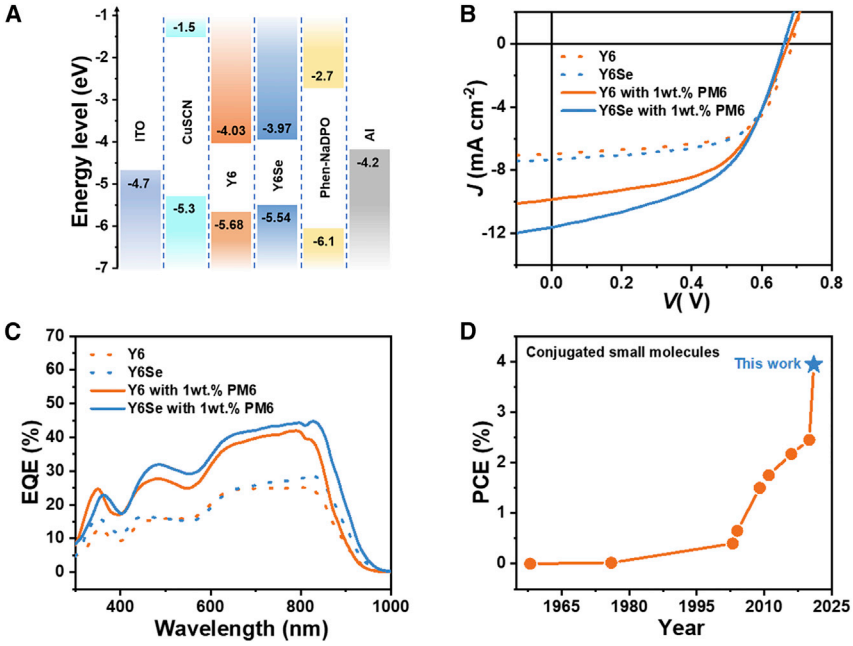

Figure 3. Energy levels and device performance

(A) Energy diagram relative to the vacuum level.

(B and C) (B) *J-V* curves and (C) EQE spectra of the SPM-OSCs based on different active layer with CuSCN/NaSCN as HTL.

(D) Efficiency evolution of SPM-OSCs based on conjugated small molecules, and the detailed parameters are summarized in Table S1.

range of the Y6 and Y6Se film, confirming there is free carrier originating from the exciton spontaneous dissociation of Y6 or Y6Se film. These results indicate that charge generation is derived from both exciton spontaneous dissociation and exciton dissociation at the CuSCN/Y6 or Y6Se interface in CuSCN-based devices. Compared with Y6-based devices with PEDOT:PSS HTL (0.22 mA cm^{-2}), the higher J_{SC} (0.63 mA cm^{-2}) and higher EQE of Y6Se-based devices supported more effective free carrier generation within SPM-OSC based on Y6Se film at room temperature (Figure S4B). Moreover, the J_{SC} of Y6Se is one order of magnitude higher than that (0.047 mA cm^{-2}) of devices based on ITIC with higher E_a (70.4 meV).[31] These results indicated more effective free carrier generation in Y6Se can be attributed to faster relaxation of exciton state or the intermediate i-Ex state as mentioned above.

MPC measurement was further carried out to investigate the charge separation within neat Y6- or Y6Se-based devices with the structure of ITO/CuSCN/NaSCN/Y6 or Y6Se/Phen-NaDPO/Al. Relatively small (~0.1%) but significant change in photocurrent is induced by applying a magnetic field of 150 mT (Figure 4A), indicating a small fraction of e-h pair, i-Ex state, and/or CT state could be observed in both Y6- and Y6Se-based devices before they have dissociated to free charge carriers. The weakly bounded e-h pair (or i-Ex state and/or CT state) contains two spin-1/2 particles, in which the applied magnetic field would alter its configuration between singlet and triplet and consequently change the photocurrent in devices. Relative to Y6, Y6Se-based device showed a broader MPC response with a larger full width at half maximum (FWHM) of 112 mT (versus 72 mT for Y6-based device) under illumination (Figure 4A), which indicated short-lived characteristics of e-h pairs (or i-Ex state and/or CT state) within Y6Se, as the singlet-triplet conversion requires a high spin precession frequency and thus reaches saturation at a relatively large field.[44] These results

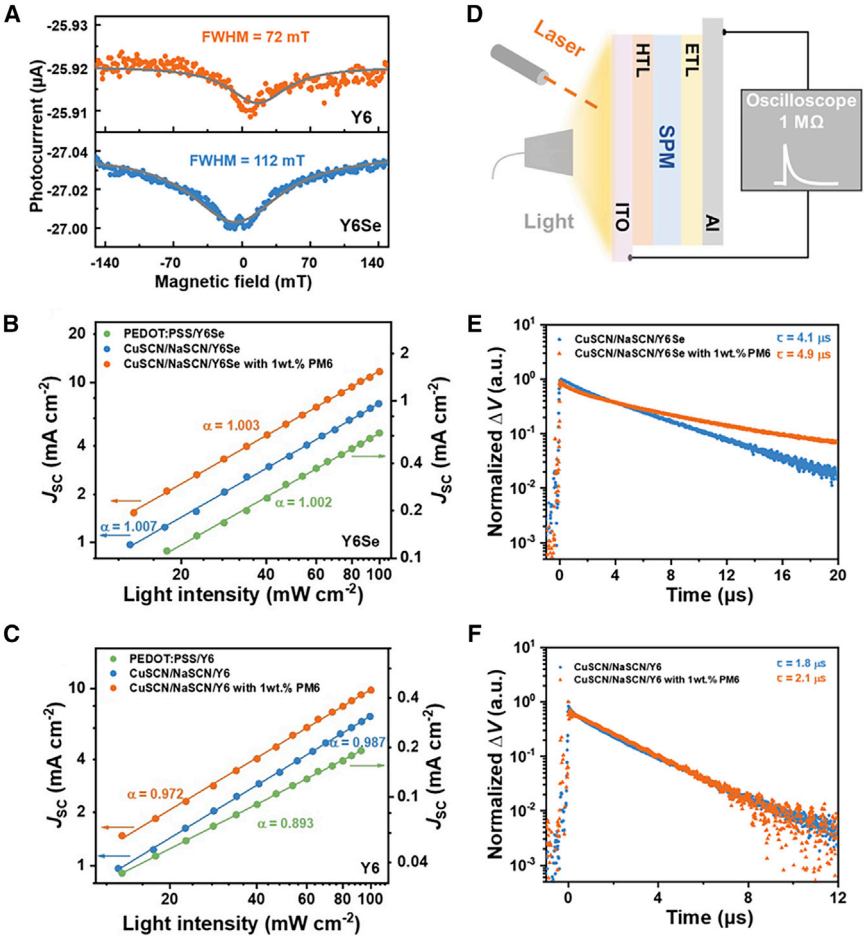

Figure 4. Exciton dissociation, charge-carrier recombination/diffusion

(A–C) (A) Magneto-photocurrent of Y6- and Y6Se-based SPM-OSCs, the solid lines are Lorentzian fits. Light intensity dependence of J_{SC} of the SPM-OSCs based on Y6Se (B) and Y6 (C) with PEDOT:PSS or CuSCN/NaSCN as HTLs.

(D–F) (D) Schematic illustration of the TPV setup. TPV curves of the SPM-OSCs based on Y6Se (E) and Y6 (F) with CuSCN/NaSCN as HTLs, with and without 1 wt % PM6 additive.

supported that shorter lifetime of e-h pairs (or i-Ex state and/or CT state) in Y6Se-based devices contributed to higher J_{SC}, compared with Y6-based control devices.

Charge-carrier recombination and diffusion

Free charge carrier generated by exciton dissociation can only contribute to the photocurrent when they are collected by the corresponding electrodes. The efficiency of charge extraction is primarily determined by the kinetic competition between bimolecular recombination and charge transport.[45] First, light intensity (P) dependent J_{SC} was investigated to understand the charge recombination behavior in the devices. The correlation of J_{SC} and P can be described as $J_{SC} \propto P^{\alpha}$. When α is closer to 1, it indicates that bimolecular recombination is negligible.[46] Remarkably, there is almost no bimolecular recombination in all Y6Se-based devices ($\alpha = 1$, Figure 4B), independent of HTL layer. In contrast, the fitted α value was as low as 0.893 for Y6-based devices with PEDOT:PSS HTL, and then Y6-based devices with CuSCN/NaSCN HTLs still exhibited α values of 0.987 (Figure 4C). Typically, bimolecular recombination process results from radiative recombination between unbound electrons and holes in direct-gap semiconductors.[47] Then the radiative recombination rate constant (k_r) is proportional to E_g|

$P_{cv}|^2$, where E_g is bandgap and $|P_{cv}|^2$ is the interband transition matrix element. $|P_{cv}|^2$ is positively related to E_b.[48–50] These results indicated that the negligible bimolecular recombination of Y6Se can be attributed to low E_b. Then, we studied the transport/diffusion properties of free carriers. The carrier diffusion length (L_D) was calculated according to Equation 2[51]:

$$L_D = \sqrt{\frac{k_B T}{e}\mu\tau} \quad \text{(Equation 2)}$$

where k_B is Boltzmann's constant, T is the temperature, μ is the carrier mobility, and τ is the carrier lifetime. TPV measurements were used to study the charge-carrier lifetime by recording the transient voltage decay of the device under open-circuit conditions under continuous illumination before a small perturbative light pulse was injected (Figure 4D).[52] The charge-carrier lifetime of Y6Se-based devices with CuSCN HTL is 4.1 μs (Figure 4E), which is higher than that (1.8 μs) of Y6-based devices (Figure 4F). These results indicated slower charge-carrier recombination occurred within the Y6Se-based devices than the Y6 based ones. The enhanced charge-carrier lifetime within Y6Se can be attributed to the lower trap density of Y6Se calculated from space-charge-limited-current measurement (Y6Se: 5.1×10^{16} cm^{-3} versus Y6: 6.4×10^{16} cm^{-3}).[25] In our device configuration, most excitons generated and dissociated at the side away from the cathode, thus electron diffusion length is critical to charge-carrier extraction. The electron mobility of Y6 and Y6Se are 1.7×10^{-4} cm^2 V^{-1} s^{-1} and 2.7×10^{-4} cm^2 V^{-1} s^{-1}, respectively.[25] The electron diffusion length of Y6Se is 53 nm in CuSCN-based devices, while the electron diffusion length of Y6 is only 29 nm. In addition to negligible bimolecular recombination, the longer charge-carrier lifetime and electron diffusion length within Y6Se film, which benefited charge extraction in the device, contributed to the higher photocurrent and efficiency of SPM-OSCs based on Y6Se, relative to the Y6-based control device.

The effect of the hole transporting polymer

Moreover, the devices based on Y6Se with 1wt % hole transporting polymer (PM6, Figure S5) demonstrated a PCE of 3.94% with a J_{SC} of 11.61 mA cm^{-2}, higher than those (PCE of 3.70% and J_{SC} of 9.85 mA cm^{-2}) of the devices based on Y6 (Figure 3B). Compared with the devices based on Y6 (42%), the corresponding maximum EQE based on Y6Se devices is increased to 45% (Figure 3C). The PCE of 3.94% is significantly higher than those values reported for SPM-OSCs based on single photovoltaic small molecules in the literature (Figure 3D). To explain how PM6 improves the device performance, we evaluated the variation of hole mobility, PL intensity, and carrier lifetime after adding 1wt % PM6. The organic field-effect transistor (OFETs)-based Y6Se (6.7×10^{-3} cm^2 V^{-1} s^{-1}) and Y6Se with 1wt % PM6 (7.0×10^{-3} cm^2 V^{-1} s^{-1}) displayed similar hole mobilities (Figure S6). Compared with pure Y6Se film, Y6Se with 1wt % PM6 film showed slightly PL quenching (~7%) at the same film thickness resulting from hole transfer from Y6Se to PM6 (Figure S7). Therefore, slightly enhanced hole mobility and hole transfer may not be the main factors for improved PCE. Moreover, with the addition of 1wt % PM6, both Y6- and Y6Se-based devices showed the obviously increased charge-carrier lifetime to 2.1 μs or 4.9 μs, respectively (Figures 4E–4F), which resulted the extended electron diffusion length (Y6: 30 nm and Y6Se: 59 nm). It should be noted here the increased charge-carrier lifetime by adding small amounts of polymer may be relevant to trap passivation and/or suppressing Langevin recombination, which requires more investigations in the future. Along with negligible bimolecular recombination (Figures 4B–4C), the enhanced electron diffusion lengths should be the dominated factor for improved EQE and PCE in devices with 1wt % PM6 additive.

Thermal stability

In addition, we compared the stability of Y6Se-based SPM-OSCs and BHJ-OSCs under thermal annealing. As-cast Y6Se-based SPM-OSCs with CuSCN HTL maintained around 96% of its initial PCE after 30 min heating at 85°C (Figure S8A left). The slight attenuation of device performance was attributed to the decrease of open-circuit voltage (V_{OC}), which could be seen in Figure S8B–S8D left. Polymer additive obviously accelerated the device degradation under thermal annealing (Figure S8). At the same thermal pressure, the BHJ-OSCs with blend active layer of PM6:Y6Se (1:1.2, *w/w*) showed a sharp degradation to only around 20% of its initial PCE (Figure S8A left). After heating at 85°C for 60 h, the PCE of SPM-OSCs still remained around 67% of the initial value (Figure S8A right), along with V_{OC}, J_{SC}, and fill factor maintained 85%, 93%, and 80% of the initial value, respectively (Figure S8B–S8D right), which can be attributed to stable active layer morphology in SPM-OSCs based on neat active layer.

In summary, the detailed exciton dissociation kinetic studies supported exciton dissociation of Y6Se was easier than Y6. Then, the SPM-OSCs based on Y6Se show long charge-carrier lifetime and extended electron diffusion length, leading to high EQE and PCEs. The PCE was further improved to 3.94% with a maximum EQE value of 45% by further extended electron diffusion by using 1wt % PM6 additive in Y6Se active layer. To our knowledge, the 3.94% PCE is the record value reported for SPM-OSCs based on D-A small molecules. The impressively improved device efficiency and very good thermal stability of SPM-OSCs achieved in this study boost us to believe the SPM-OSCs provide a promising option for OSC commercialization. Further, developing photovoltaic materials with lower E_b and higher free charge-carrier diffusion length (carrier mobility and lifetime) should be critical for SPM-OSCs in future. In particular, if E_b can be reduced to ~25 meV (the thermal energy at room temperature) by molecular engineering, such as turning the symmetric backbone into an asymmetric structure, introducing polar groups, etc., the exciton will spontaneously dissociate into free charges like inorganic semiconductors. Moreover, long carrier diffusion length can be achieved by designing high carrier mobility and long carrier lifetime materials with improved intermolecular interaction and low trap density. The SPM-OSCs should be capable of achieving high efficiencies comparable to those of commercial inorganic solar cells, given that exciton dissociation and charge-carrier diffusion within single organic photovoltaic semiconductors is efficient enough.

EXPERIMENTAL PROCEDURES

Resource availability

Lead contact

Further information and requests for resources should be directed to and will be fulfilled by the lead contact, Yuze Lin (linyz@iccas.ac.cn).

Materials availability

No new materials were generated within this work. The full chemical names of active layer materials used in this work are provided in Note S1. PM6 was purchased form Solarmer Materials Inc. Y6 was purchased from eFlexPV Ltd. Y6Se was synthesized according to the literature procedures.[25] CuSCN and diethyl sulfide (DES) were purchased from Tokyo Chemical Industry. NaSCN was purchased from J&K Scientific Ltd. Phen-NaDPO was purchased from PURI Materials Technologies Co., Ltd.

Data and code availability

All data reported in this paper will be shared by the lead contact on request. This paper does not report original code. Any additional information required to reanalyze the data reported in this paper is available from the lead contact on request.

Theoretical methodology

The molecular geometries were optimized by DFT at the B3LYP/6-31G(d,p) level. To obtain a reliable description, the electronic properties were then calculated by DFT and time-dependent DFT (TDDFT) with the long-range-corrected (LRC) functional ωB97X and the 6-311G(d,p) basis set. Moreover, the range separation parameter (ω) of the LRC functional was optimized by a gap-tuning procedure; namely, the ω value was determined by minimizing the value of J^2 (ω):

$$J^2 = \sum_{i=0}^{1}[\varepsilon_H(N+i) + IP(N+i)]^2 \quad \text{(Equation 3)}$$

Here, ε_H denotes the HOMO energy of a given molecule; N is the number of electrons in the neutral molecule. Hereafter, the optimally tuned range-separated functional is labeled as ωB97X*.

To take account of the impact of surrounding dielectric medium (electronic polarization effect), the polarizable continuum model was incorporated in the DFT/TDDFT calculations. The dielectric constants (ε) of the studied compounds were obtained according to the Clausius-Mossotti equation:

$$\frac{\varepsilon - 1}{\varepsilon + 2} = \frac{4\pi}{3}\frac{\alpha}{V} \quad \text{(Equation 4)}$$

Here, α is the isotropic component of the molecular polarizability, and V is the volume occupied by a single molecule, which were calculated by Multiwfn software at the tuned ωB97X*/6-311G(d,p) level in the gas phase. Then the ω value was optimized again in the presence of dielectrics to calculate the related energies in solid state. All the calculations were carried out with the Gaussian 16 package.[53]

UPS and LEIPS spectroscopy

UPS spectra were obtained from AXIS ULTRA DLD (Kratos) with He I (21.22 eV) excitation lines and a sample bias of −9 V under a vacuum of 3.0×10^{-8} Torr. LEIPS measurement was performed on a customized ULVAC-PHI LEIPS instrument with Bremsstrahlung isochromatic mode. The Y6Se film was prepared by spin-coating Y6Se chloroform solution (10 mg mL^{-1}) at 3,000 rpm for 40 s on the ITO substrate.

Steady-state photoluminescence spectroscopy measurements

PL spectra were measured with a FLS980 fluorescence spectrophotometer. Y6Se without and with 1wt % PM6 solution (22 mg mL^{-1}) were spin-coated from chloroform solution at 3,000 rpm for 40 s on the quartz substrate.

Temperature-dependent photoluminescence spectroscopy measurements

The Y6Se solutions (20 mg mL^{-1} in chloroform) was spin-coated on the quartz substrate. Temperature-dependent photoluminescence spectra were measured by micro-Raman spectrometer (Horiba-JY HR Evolution), with the excitation laser wavelength of 633 nm and the signal was collected through a ×50 objective. The total power of the laser spot under objective was approximately 0.35 μW, ~10 W/cm^2 considering a laser spot diameter of ~2 μm. A cryostat (from Cryo Industry of America) was used to provide a vacuum environment and continuous temperature control from 80 to 300 K by liquid nitrogen flow.

Time-resolved photoluminescence spectroscopy measurements

To investigate the fluorescence lifetime of Y6 and Y6Se, we used an ultrafast Er-fiber laser (1560 ± 10 nm, 80 MHz, ~80 fs) and two frequency doubling crystals to generate ~390 nm pulsed laser for excitation. The signal was collected by a ×100

objective (Nikon, NA = 0.90) with the back-scattering mode. The reflected laser is blocked by a 405-nm long-pass filter and the emission light through an 888-nm band-pass filter to a SPAD detector. Single-photon counting was performed with a PicoHarp 300 module (PicoQuant). Data analysis is based on the SymPhoTime 64 software. The excitation power was ~45 W/cm^2.

Transient absorption spectroscopy measurements

The transient absorption (TA) setup was built based on a Pharos laser system as the laser source and a Femto-100 spectrometer (TimeTech LLC) as the spectrometer. The center wavelength of the Pharos output beam was around 1,030 nm, and the pulse repetition rate of this beam was 100 KHz. The fundamental beam was split into two beams, one part was used to pump an optical parametric amplifier (OPA; TOPAS) to generate the wavelength-tunable excitation pulses. The other beam was sent through a delay stage using a motorized translation stage to generate the probe pulse. The probe was generated by focusing an attenuated 1,030 nm beam into a CaF_2 window for probing range of 350 to 650 nm or a Nd:YAG crystal for probing range of 500 to 950 nm and 1,150 to 1,650 nm. The pump beam was chopped at frequency of 500 Hz and its intensity was tuned by a neutral density filter wheel. The pump and probe beams were spatially overlapped on the surface of the sample. The transmitted probe beam was directed to the multichannel CMOS sensors by an optical fiber, while the transmitted pump beam was stopped by a beam blocker.

Fabrication and Characterization of SPM-OSCs

SPM-OSCs were fabricated with the structure of ITO/HTLs/Y6 or Y6Se/ Phen-NaDPO (5 nm)/Al (100 nm). A PEDOT:PSS (30 nm) layer was deposited through spin-coating on precleaned ITO-coated glass and dried subsequently at 150°C for 15 min in air. The CuSCN solution, which was prepared by dissolving CuSCN powder in DES (35 mg mL^{-1}) at 60°C for 12 h and then filtered with 0.22 μm polyadiohexylenediamine, was spin-coated on the ITO substrate at 2000 rpm for 40 s and then annealed at 105°C for 1 min. The NaSCN solution (2 mg mL^{-1} in isopropanol) was spin-coated on the CuSCN film (~65 nm) at 3,000 rpm for 40 s and then annealing at 105°C for 15 min in air. Then the devices with HTLs were transferred to a nitrogen glove box, and the Y6Se was dissolved in chloroform at different concentration of 18 to 24 mg mL^{-1}, then was spun on HTLs at different speed for 40 s to obtain Y6Se film with different thickness. The optimized film for Y6 and Y6Se with approximately 85 nm are obtained by spin-coating Y6 and Y6Se chloroform solution (22 mg mL^{-1}) at 3,000 rpm for 40 s. Y6 or Y6Se solution with 1wt % PM6 (22 mg mL^{-1}) solution was spin-coated from chloroform solution at 3,000 rpm for 40 s onto the HTLs. The Phen-NaDPO solution (0.5 mg mL^{-1} in isopropanol) was spin-coated on the active layer at 2,000 rpm for 40 s. Finally, Al electrode evaporated onto Phen-NaDPO under vacuum (approximately 10^{-5} Pa). The active area of the cells was 0.04 cm^2. The *J-V* curves were measured under AM1.5G illumination at 100 mW cm^{-2} using an AAA solar simulator (XES-70S1, SAN-EI Electric Co., Ltd) calibrated with a standard photovoltaic cell equipped with a KG5 filter (certified by the National Institute of Metrology) and a Keithley 2450 source-measure unit. The EQE data were obtained using a solar cell spectral response measurement system (QE-R3011, Enli Technology Co. Ltd).

Magneto-photocurrent measurements

For the magneto-photocurrent (MPC) measurements, the devices (ITO/CuSCN/NaSCN/Y6 or Y6Se/Phen-NaDPO/Al) were placed in a magnetic field B provided by an electromagnet (East Changing EM1) with B up to 150 mT. Electrical wires made of metallic alloys were used for electrode contacts to keep the parasitic magneto-resistance below 0.001%. The devices were illuminated with a 405 nm laser

diode (ocean insight LSM-405A), and the photocurrent was measured at zero bias with a multimeter (Keithley 2400) while sweeping the field back and forth for several cycles to improve the S/N ratio.

Transient photovoltage measurements

For transient photovoltage measurements, an attenuated 810 nm laser pulse with a pulse width of 35 fs was used as a small perturbation, a halogen lamp with 100 mW cm^{-2} as the background illumination. Devices were connected to the oscilloscope (MDO3104) using a 1 MΩ input impedance to form the open-circuit condition.

Fabrication and characterization of OFETs

OFET devices were fabricated on a commercial Si/SiO_2/Au substrate purchased from First MEMS Co. Ltd. A heavily doped n-type Si wafer and a layer of dry oxidized SiO_2 (300 nm, with roughness lower than 0.1 nm and capacitance of 11 nF cm^{-2}) were used as a gate electrode and gate dielectric layer, respectively. The drain-source (D-S) gold contacts were fabricated by photolithography. Before deposition of the organic semiconductor, the gate dielectrics were treated with octadecyltrichlorosilane (OTS) in a vacuum oven at a temperature of 120°C, forming OTS self-assembled monolayers. The treated substrates were rinsed successively with hexane, chloroform, and isopropyl alcohol. Then, Y6Se without and with 1wt % PM6 chloroform solution was spin-coated on the substrate at 3,000 rpm for 30 s with the concentration of 22 mg mL^{-1}. The devices were measured on a FS-Pro semiconductor parameter analyzer at room temperature. The mobilities were calculated from the saturation region with the following equation: $I_D^{0.5} = (C_i \mu W/2L)^{0.5}(V_G\text{-}V_T)$, where I_D is the drain-source current, W is the channel width (1400 μm), L is the channel length (10 μm), μ is the field-effect mobility, C_i is the capacitance per unit area of the gate dielectric layer, and V_G and V_T are the gate voltage and threshold voltage, respectively.

Stability tests

For thermal stability test, the devices were fabricated with the structure of ITO/CuSCN/active layer/Phen-NaDPO/Al. The SPM-OSCs was fabricated by spin-coating the Y6Se without and with 1wt % PM6 solution (22 mg mL^{-1}) at 3,000 rpm for 40 s onto the CuSCN layer. The BHJ-OSCs were fabricated by spin-coating PM6:Y6Se (1:1.2, *w*/*w*, 16 mg mL^{-1} in total) blending solution at 3,000 rpm for 40 s onto the CuSCN layer. The preparation methods of CuSCN, Phen-NaDPO, and Al layers are the same as the above description (see Fabrication and Characterization of SPM-OSCs). Then the devices were heated at 85°C in a nitrogen glove box. The photovoltaic parameters were recorded by a Keithley 2450 source meter.

SUPPLEMENTAL INFORMATION

Supplemental information can be found online at https://doi.org/10.1016/j.xcrp.2022.100895.

ACKNOWLEDGMENTS

We acknowledge financial support from the National Natural Science Foundation of China (52173189, 21873048), the Natural Science Foundation of Jiangsu Province (BK20180319).

AUTHOR CONTRIBUTIONS

Y. Lin conceived the idea, designed the experiments, and supervised the study. Z.Z. fabricated organic solar cells and analyzed data. L.L. and W.X. performed temperature-dependent PL and TRPL measurements and analysis. C.X. and Y. Yang

performed TA measurements and analysis. P.J. and C.Z. performed MPC measurements and analysis. M.H. and Y. Yi were responsible for the DFT and TDDFT calculations and analysis. H.W. contributed to temperature-dependent PL and TPV measurements. Y. Li performed TPV and OFET measurements and analysis. Y.Lin and Z.Z. wrote the paper. All authors reviewed this paper. Z.Z. and L.L. contributed equally to this work.

DECLARATION OF INTERESTS

The authors declare no competing interests.

Received: September 30, 2021
Revised: March 16, 2022
Accepted: April 20, 2022
Published: May 11, 2022

REFERENCES

1. Zhang, J., Tan, H.S., Guo, X., Facchetti, A., and Yan, H. (2018). Material insights and challenges for non-fullerene organic solar cells based on small molecular acceptors. Nat. Energ. *3*, 720–731. https://doi.org/10.1038/s41560-018-0181-5.

2. Cheng, P., Li, G., Zhan, X., and Yang, Y. (2018). Next-generation organic photovoltaics based on non-fullerene acceptors. Nat. Photon. *12*, 131–142. https://doi.org/10.1038/s41566-018-0104-9.

3. Fukuda, K., Yu, K., and Someya, T. (2020). The future of flexible organic solar cells. Adv. Energ. Mater. *10*, 2000765. https://doi.org/10.1002/aenm.202000765.

4. Zhang, Y., Ng, S.W., Lu, X., and Zheng, Z. (2020). Solution-Processed transparent electrodes for emerging thin-film solar cells. Chem. Rev. *120*, 2049–2122. https://doi.org/10.1021/acs.chemrev.9b00483.

5. Park, S., Heo, S.W., Lee, W., Inoue, D., Jiang, Z., Yu, K., Jinno, H., Hashizume, D., Sekino, M., Yokota, T., et al. (2018). Self-powered ultra-flexible electronics via nano-grating-patterned organic photovoltaics. Nature *561*, 516–521. https://doi.org/10.1038/s41586-018-0536-x.

6. Li, C., Zhou, J., Song, J., Xu, J., Zhang, H., Zhang, X., Guo, J., Zhu, L., Wei, D., Han, G., et al. (2021). Non-fullerene acceptors with branched side chains and improved molecular packing to exceed 18% efficiency in organic solar cells. Nat. Energ. *6*, 605–613. https://doi.org/10.1038/s41560-021-00820-x.

7. Liu, Q., Jiang, Y., Jin, K., Qin, J., Xu, J., Li, W., Xiong, J., Liu, J., Xiao, Z., Sun, K., et al. (2020). 18% efficiency organic solar cells. Sci. Bull. *65*, 272–275. https://doi.org/10.1016/j.scib.2020.01.001.

8. Zhu, L., Yi, Y., and Wei, Z. (2018). Exciton binding energies of nonfullerene small molecule acceptors: implication for exciton dissociation driving forces in organic solar cells. J. Phys. Chem. C *122*, 22309–22316. https://doi.org/10.1021/acs.jpcc.8b07197.

9. Kraner, S., Scholz, R., Koerner, C., and Leo, K. (2015). Design proposals for organic materials exhibiting a low exciton binding energy. J. Phys. Chem. C *119*, 22820–22825. https://doi.org/10.1021/acs.jpcc.5b07097.

10. Clarke, T.M., and Durrant, J.R. (2010). Charge photogeneration in organic solar cells. Chem. Rev. *110*, 6736–6767. https://doi.org/10.1021/cr900271s.

11. Benatto, L., Sousa, K.R.d.A., and Koehler, M. (2020). Driving force for exciton dissociation in organic solar cells: the influence of donor and acceptor relative orientation. J. Phys. Chem. C *124*, 13580–13591. https://doi.org/10.1021/acs.jpcc.0c03116.

12. Li, Y., Li, T., and Lin, Y. (2021). Stability: next focus in organic solar cells based on non-fullerene acceptors. Mater. Chem. Front. *5*, 2907–2930. https://doi.org/10.1039/d1qm00027f.

13. Zhao, F., Zhang, H., Zhang, R., Yuan, J., He, D., Zou, Y., and Gao, F. (2020). Emerging approaches in enhancing the efficiency and stability in non-fullerene organic solar cells. Adv. Energ. Mater. *10*, 2002746. https://doi.org/10.1002/aenm.202002746.

14. Cheng, P., and Zhan, X. (2016). Stability of organic solar cells: challenges and strategies. Chem. Soc. Rev. *45*, 2544–2582. https://doi.org/10.1039/c5cs00593k.

15. Duan, L., and Uddin, A. (2020). Progress in stability of organic solar cells. Adv. Sci. *7*, 1903259. https://doi.org/10.1002/advs.201903259.

16. He, Y., Li, N., and Brabec, C.J. (2021). Single-component organic solar cells with competitive performance. Org. Mater. *03*, 228–244. https://doi.org/10.1055/s-0041-1727234.

17. Zhang, Y., Deng, D., Wu, Q., Mi, Y., Yang, C., Zhang, X., Yang, Y., Zou, W., Zhang, J., Zhu, L., et al. (2020). High-efficient charge generation in single-donor-component-based p-i-n structure organic solar cells. Solar RRL *4*, 1900580. https://doi.org/10.1002/solr.201900580.

18. Firdaus, Y., Le Corre, V.M., Karuthedath, S., Liu, W., Markina, A., Huang, W., Chattopadhyay, S., Nahid, M.M., Nugraha, M.I., Lin, Y., et al. (2020). Long-range exciton diffusion in molecular non-fullerene acceptors. Nat. Commun. *11*, 5220. https://doi.org/10.1038/s41467-020-19029-9.

19. Park, S.H., Kim, Y., Kwon, N.Y., Lee, Y.W., Woo, H.Y., Chae, W.S., Park, S., Cho, M.J., and Choi, D.H. (2020). Significantly improved morphology and efficiency of nonhalogenated solvent-processed solar cells derived from a conjugated donor-acceptor block copolymer. Adv. Sci. *7*, 1902470. https://doi.org/10.1002/advs.201902470.

20. Jiang, X., Yang, J., Karuthedath, S., Li, J., Lai, W., Li, C., Xiao, C., Ye, L., Ma, Z., Tang, Z., and Laquai, F. (2020). Miscibility-controlled phase separation in double-cable conjugated polymers for single-component organic solar cells with efficiencies over 8%. Angew. Chem. Int. Ed. *59*, 21683–21692. https://doi.org/10.1002/anie.202009272.

21. Wang, W., Sun, R., Guo, J., Guo, J., and Min, J. (2019). An oligothiophene-fullerene molecule with a balanced donor-acceptor backbone for high-performance single-component organic solar cells. Angew. Chem. Int. Ed. *58*, 14556–14561. https://doi.org/10.1002/anie.201908232.

22. Liang, S., Jiang, X., Xiao, C., Li, C., Chen, Q., and Li, W. (2021). Double-cable conjugated polymers with pendant rylene diimides for single-component organic solar cells. Acc. Chem. Res. *54*, 2227–2237. https://doi.org/10.1021/acs.accounts.1c00070.

23. Lin, Y., Wang, J., Zhang, Z.G., Bai, H., Li, Y., Zhu, D., and Zhan, X. (2015). An electron acceptor challenging fullerenes for efficient polymer solar cells. Adv. Mater. *27*, 1170–1174. https://doi.org/10.1002/adma.201404317.

24. Yuan, J., Zhang, Y., Zhou, L., Zhang, G., Yip, H.-L., Lau, T.-K., Lu, X., Zhu, C., Peng, H., Johnson, P.A., et al. (2019). Single-junction organic solar cell with over 15% efficiency using fused-ring acceptor with electron-deficient core. Joule *3*, 1140–1151. https://doi.org/10.1016/j.joule.2019.01.004.

25. Zhang, Z., Li, Y., Cai, G., Zhang, Y., Lu, X., and Lin, Y. (2020). Selenium heterocyclic electron acceptor with small urbach energy for as-cast high-performance organic solar cells. J. Am.

Chem. Soc. *142*, 18741–18745. https://doi.org/10.1021/jacs.0c08557.

26. Li, T., Wu, Y., Zhou, J., Li, M., Wu, J., Hu, Q., Jia, B., Pan, X., Zhang, M., Tang, Z., et al. (2020). Butterfly effects arising from starting materials in fused-ring electron acceptors. J. Am. Chem. Soc. *142*, 20124–20133. https://doi.org/10.1021/jacs.0c09800.

27. Zhang, J., Liu, W., Zhou, G., Yi, Y., Xu, S., Liu, F., Zhu, H., and Zhu, X. (2019). Accurate determination of the minimum HOMO offset for efficient charge generation using organic semiconducting alloys. Adv. Energ. Mater. *10*, 1903298. https://doi.org/10.1002/aenm.201903298.

28. Li, Y., Qian, D., Zhong, L., Lin, J.-D., Jiang, Z.-Q., Zhang, Z.-G., Zhang, Z., Li, Y., Liao, L.-S., and Zhang, F. (2016). A fused-ring based electron acceptor for efficient non-fullerene polymer solar cells with small HOMO offset. Nano Energy *27*, 430–438. https://doi.org/10.1016/j.nanoen.2016.07.019.

29. Chen, S., Wang, Y., Zhang, L., Zhao, J., Chen, Y., Zhu, D., Yao, H., Zhang, G., Ma, W., Friend, R.H., et al. (2018). Efficient nonfullerene organic solar cells with small driving forces for both hole and electron transfer. Adv. Mater. *30*, 1804215. https://doi.org/10.1002/adma.201804215.

30. Sun, C., Qin, S., Wang, R., Chen, S., Pan, F., Qiu, B., Shang, Z., Meng, L., Zhang, C., Xiao, M., et al. (2020). High efficiency polymer solar cells with efficient hole transfer at zero highest occupied molecular orbital offset between methylated polymer donor and brominated acceptor. J. Am. Chem. Soc. *142*, 1465–1474. https://doi.org/10.1021/jacs.9b09939.

31. Zhu, L., Zhang, J., Guo, Y., Yang, C., Yi, Y., and Wei, Z. (2021). Small exciton binding energies enabling direct charge photogeneration towards low-driving-force organic solar cells. Angew. Chem. Int. Ed. *60*, 15348–15353. https://doi.org/10.1002/anie.202105156.

32. Wang, R., Zhang, C., Li, Q., Zhang, Z., Wang, X., and Xiao, M. (2020). Charge separation from an intra-moiety intermediate state in the high-performance PM6:Y6 organic photovoltaic blend. J. Am. Chem. Soc. *142*, 12751–12759. https://doi.org/10.1021/jacs.0c04890.

33. Hodgkiss, J., Price, M., Hume, P., Ilina, A., Wagner, I., Tamming, R., Thorn, K., Jiao, W., Campbell, A., Conaghan, P., et al. (2021). Free charge photogeneration in a single component high photovoltaic efficiency organic semiconductor.. Preprint. Nat. Portfolio. Posted 08 Apr, 2021. https://doi.org/10.21203/rs.3.rs-376343/v1.

34. Zhu, L., Wei, Z., and Yi, Y. (2022). Exciton binding energies in organic photovoltaic materials: a theoretical perspective. J. Phys. Chem. C *126*, 14–21. https://doi.org/10.1021/acs.jpcc.1c08898.

35. Kahn, A. (2016). Fermi level, work function and vacuum level. Mater. Horizons *3*, 7–10. https://doi.org/10.1039/c5mh00160a.

36. Li, T., Wang, K., Cai, G., Li, Y., Liu, H., Jia, Y., Zhang, Z., Lu, X., Yang, Y., and Lin, Y. (2021). Asymmetric glycolated substitution for enhanced permittivity and ecocompatibility of high-performance photovoltaic electron acceptor. JACS Au *1*, 1733–1742. https://doi.org/10.1021/jacsau.1c00306.

37. Chen, Z., Yu, C., Shum, K., Wang, J.J., Pfenninger, W., Vockic, N., Midgley, J., and Kenney, J.T. (2012). Photoluminescence study of polycrystalline $CsSnI_3$ thin films: determination of exciton binding energy. J. Lumin. *132*, 345–349. https://doi.org/10.1016/j.jlumin.2011.09.006.

38. Sun, S., Salim, T., Mathews, N., Duchamp, M., Boothroyd, C., Xing, G., Sum, T.C., and Lam, Y.M. (2014). The origin of high efficiency in low-temperature solution-processable bilayer organometal halide hybrid solar cells. Energy Environ. Sci. *7*, 399–407. https://doi.org/10.1039/c3ee43161d.

39. Wangyang, P., Gong, C., Rao, G., Hu, K., Wang, X., Yan, C., Dai, L., Wu, C., and Xiong, J. (2018). Recent advances in halide perovskite photodetectors based on different dimensional materials. Adv. Opt. Mater. *6*, 1701302. https://doi.org/10.1002/adom.201701302.

40. Eisner, F., Foot, G., Yan, J., Azzouzi, M., Georgiadou, D.G., Sit, W.Y., Firdaus, Y., Zhang, G., Lin, Y.H., Yip, H.L., et al. (2021). Emissive charge-transfer states at hybrid inorganic/organic heterojunctions enable low non-radiative recombination and high-performance photodetectors. Adv. Mater. e2104654. https://doi.org/10.1002/adma.202104654.

41. Perumal, A., Faber, H., Yaacobi-Gross, N., Pattanasattayavong, P., Burgess, C., Jha, S., McLachlan, M.A., Stavrinou, P.N., Anthopoulos, T.D., and Bradley, D.D.C. (2015). High-efficiency, solution-processed, multilayer phosphorescent organic light-emitting diodes with a copper thiocyanate hole-injection/hole-transport layer. Adv. Mater. *27*, 93–100. https://doi.org/10.1002/adma.201403914.

42. Lyu, M., Chen, J., and Park, N.-G. (2019). Improvement of efficiency and stability of CuSCN-based inverted perovskite solar cells by post-treatment with potassium thiocyanate. J. Solid State Chem. *269*, 367–374. https://doi.org/10.1016/j.jssc.2018.10.014.

43. Tan, W.-Y., Wang, R., Li, M., Liu, G., Chen, P., Li, X.-C., Lu, S.-M., Zhu, H.L., Peng, Q.-M., Zhu, X.-H., et al. (2014). Lending triarylphosphine oxide to phenanthroline: a facile approach to high-performance organic small-molecule cathode interfacial material for organic photovoltaics utilizing air-stable cathodes. Adv. Funct. Mater. *24*, 6540–6547. https://doi.org/10.1002/adfm.201401685.

44. Zhang, C., Sun, D., Sheng, C.X., Zhai, Y.X., Mielczarek, K., Zakhidov, A., and Vardeny, Z.V. (2015). Magnetic field effects in hybrid perovskite devices. Nat. Phys. *11*, 427–434. https://doi.org/10.1038/nphys3277.

45. Wu, J., Cha, H., Du, T., Dong, Y., Xu, W., Lin, C.T., and Durrant, J.R. (2022). A comparison of charge carrier dynamics in organic and perovskite solar cells. Adv. Mater. *34*, e2101833. https://doi.org/10.1002/adma.202101833.

46. Mandoc, M.M., Veurman, W., Koster, L.J.A., de Boer, B., and Blom, P.W.M. (2007). Origin of the reduced fill factor and photocurrent in MDMO-PPV:PCNEPV all-polymer solar cells. Adv. Funct. Mater. *17*, 2167–2173. https://doi.org/10.1002/adfm.200601110.

47. Davies, C.L., Filip, M.R., Patel, J.B., Crothers, T.W., Verdi, C., Wright, A.D., Milot, R.L., Giustino, F., Johnston, M.B., and Herz, L.M. (2018). Bimolecular recombination in methylammonium lead triiodide perovskite is an inverse absorption process. Nat. Commun. *9*, 293. https://doi.org/10.1038/s41467-017-02670-2.

48. Sestu, N., Cadelano, M., Sarritzu, V., Chen, F., Marongiu, D., Piras, R., Mainas, M., Quochi, F., Saba, M., Mura, A., and Bongiovanni, G. (2015). Absorption F-sum rule for the exciton binding energy in methylammonium lead halide perovskites. J. Phys. Chem. Lett. *6*, 4566–4572. https://doi.org/10.1021/acs.jpclett.5b02099.

49. Elliott, R.J. (1957). Intensity of optical absorption by excitons. Phys. Rev. *108*, 1384–1389. https://doi.org/10.1103/physrev.108.1384.

50. Yang, Y., Yang, M., Li, Z., Crisp, R., Zhu, K., and Beard, M.C. (2015). Comparison of recombination dynamics in $CH_3NH_3PbBr_3$ and $CH_3NH_3PbI_3$ perovskite films: influence of exciton binding energy. J. Phys. Chem. Lett. *6*, 4688–4692. https://doi.org/10.1021/acs.jpclett.5b02290.

51. Shi, D., Adinolfi, V., Comin, R., Yuan, M., Alarousu, E., Buin, A., Chen, Y., Hoogland, S., Rothenberger, A., Katsiev, K., et al. (2015). Low trap-state density and long carrier diffusion in organolead trihalide perovskite single crystals. Science *347*, 519–522. https://doi.org/10.1126/science.aaa2725.

52. Shuttle, C.G., O'Regan, B., Ballantyne, A.M., Nelson, J., Bradley, D.D.C., de Mello, J., and Durrant, J.R. (2008). Experimental determination of the rate law for charge carrier decay in a polythiophene: fullerene solar cell. Appl. Phys. Lett. *92*, 093311. https://doi.org/10.1063/1.2891871.

53. Frisch, M.J., Trucks, G.W., Schlegel, H.B., Scuseria, G.E., Robb, M.A., Cheeseman, J.R., Scalmani, G., Barone, V., Mennucci, B., Petersson, G.A., et al. (2016). Gaussian 16, Revision A.03. https://gaussian.com.